ADVANCES IN ATMOSPHERIC SCIENCES, VOL. 38, DECEMBER 2021, 2183–2200

• **Original Paper** •

On the Diurnal Cycle of Heavy Rainfall over the Sichuan Basin during 10–18 August 2020※

Rudi XIA[1], Yali LUO[*1], Da-Lin ZHANG[1,2], Mingxin LI[1], Xinghua BAO[1], and Jisong SUN[1]

[1]*State Key Laboratory of Severe Weather*, *Chinese Academy of Meteorological Sciences*, *Beijing* 100081, *China*

[2]*Department of Atmospheric and Oceanic Science*, *University of Maryland*, *College Park*, *College Park*, *Maryland* 20742, *USA*

(Received 24 March 2021; revised 12 October 2021; accepted 14 October 2021)

ABSTRACT

A sustained heavy rainfall event occurred over the Sichuan basin in southwest China during 10–18 August 2020, showing pronounced diurnal rainfall variations with nighttime peak and afternoon minimum values, except on the first day. Results show that the westward extension of the anomalously strong western Pacific subtropical high was conducive to the maintenance of a southerly low-level jet (LLJ) in and to the southeast of the basin, which favored continuous water vapor transport and abnormally high precipitable water in the basin. The diurnal cycle of rainfall over the basin was closely related to the periodic oscillation of the LLJ in both wind speed and direction that was caused by the combination of inertial oscillation and terrain thermal forcing. The nocturnally enhanced rainfall was produced by moist convection mostly initiated during the evening hours over the southwest part of the basin where high convective available potential energy with moister near-surface moist air was present. The convective initiation took place as cold air from either previous precipitating clouds from the western Sichuan Plateau or a larger-scale northerly flow met a warm and humid current from the south. It was the slantwise lifting of the warm, moist airflow above the cold air, often facilitated by southwest vortices and quasi-geostrophic ascent, that released the convective instability and produced heavy rainfall.

Key words: diurnal cycle, heavy rainfall, low-level jet, inertial oscillation, terrain, Sichuan basin

Citation: Xia, R. D., Y. L. Luo, D.-L. Zhang, M. X. Li, X. H. Bao, and J. S. Sun, 2021: On the diurnal cycle of heavy rainfall over the Sichuan Basin during 10–18 August 2020. *Adv. Atmos. Sci.*, **38**(12), 2183–2200, https://doi.org/10.1007/s00376-021-1118-7.

Article Highlights:

- The diurnal cycle of rainfall with higher nocturnal amount over the basin was closely related to the periodic oscillation of a LLJ.
- The periodic oscillation of the LLJ was caused by the combination of inertial oscillation and terrain thermal forcing.
- The nocturnal rainfall was enhanced by convective storms initiated over the southwest of the basin during evening hours.
- The convective initiation occurred as cold air from either previous precipitating clouds or a larger-scale northerly flow met a warm and humid current from the south.

1. Introduction

The Sichuan basin in southwest China is located on the southeast side of the Qinghai-Tibet Plateau, with Mt. Daba in the northeast, Mt. Dalou in the southeast, the Yunnan-Guizhou Plateau to the south, the Hengduan Cordillera to the southwest, and the western Sichuan Plateau to the west (Fig. 1). This region suffers from frequent occurrences of heavy rainfall in summer (Chen et al., 2013; Luo et al., 2020), which have often caused geological disasters such as landslides and flash floods leading to serious casualties and economic losses.

Previous studies have shown the importance of large-scale pressure systems such as the western Pacific subtropical high, the South Asian high, the Asian monsoon and mid-latitude troughs in the generation of heavy rainfall over the Sichuan basin (Ueno et al., 2011; Luo et al., 2020). The southwest vortex—a low-pressure cyclonic system mainly evident in the lower troposphere—is thought to be the most important mesoscale system causing heavy rainfall in the Sichuan basin (e.g., Fu et al., 2014, 2019; Feng et al., 2016). The formation of the southwest vortex is closely related to the topography of the Qinghai-Tibet Plateau (Wang and Tan, 2014), and the movement of the Tibet-Plateau vortex

※ This paper is a contribution to the special issue on Summer 2020: Record Rainfall in Asia—Mechanisms, Predictability and Impacts.

* Corresponding author: Yali LUO
Email: ylluo@cma.gov.cn; yali.luo@qq.com

out of the plateau (Li et al., 2017).

A unique feature of rainfall over the Sichuan basin is a prominent peak from late night to early morning in its diurnal variation, differing from many other regions in China (Yuan et al., 2012; Jin et al., 2013; Xia et al., 2015; Luo et al., 2016). Previous studies suggested that the diurnal rainfall cycle in the Sichuan basin is closely related to the regional mountain-plain solenoids driven by the differential solar heating between the surrounding mountains and the basin (Bao et al., 2011; Qian et al., 2015) in association with a south-southwesterly low-level jet (LLJ) in the planetary boundary layer (PBL) to the southeast of the basin (Jin et al., 2013). That is, the convergence of downslope winds mainly to the west of the basin driven by the terrain thermal forcing and the warm, moist air transported by the south-southwesterly LLJ contributed greatly to the nocturnal rainfall peak over the basin. The nocturnal enhancement of LLJs has been observed over many regions worldwide, and explained using the inertial oscillation theory (Blackadar, 1957) and the terrain thermal forcing theory (Holton, 1967), respectively, or their combinations (Zhang et al., 2006; Jiang et al., 2007; Du and Rotunno, 2014; Shapiro et al., 2016). The basis of the inertial oscillation theory lies in the sudden reduction in eddy viscosity at sunset due to stabilization of the PBL, which is mainly a result of radiative cooling of the land surface (Blackadar, 1957; Buajitti and Blackadar, 1957; Hoxit, 1975; Zhang et al., 2006). The decoupling of the middle and upper portion of the PBL from the surface leads to the development of supergeostrophic winds during nighttime. The terrain thermal forcing theory, which most likely plays a secondary role (Du and Rotunno, 2014; Shapiro et al., 2016), highlights the important role of differential heating and cooling over sloping terrains, which causes the diurnal buoyancy-driven flow over the sloping terrain. The Coriolis force can generate an oscillation of the horizontal wind and acquires a southerly component several hours later after the westward wind component formed on the east side of a mountain range sloping upward from the east to west. Recently, Zhang et al. (2019, hereafter Z19) applied the inertial oscillation theory to clarifying the nocturnal enhancement of LLJs southeast of the Sichuan basin. They found that the nocturnal enhancement of the south-southwesterly LLJ resulted in a nighttime peak of net moisture flux into the basin at around 2200 LST, which was about four hours before the nighttime rainfall peak. The night-time downslope wind on the eastern Qinghai-Tibet Plateau and the northern Yunnan-Guizhou Plateau, controlled by shallow thermal forcing, was found to contribute only a small portion of moisture flux into the basin (Z19).

The nighttime rainfall enhancement over the Sichuan basin could be contributed by heavy-rain-producing systems that originate over the eastern side of the Qinghai-Tibet Plateau and the northern side of the Yunnan-Guizhou Plateau and then move into the basin (Wang et al., 2005; Bao et al., 2011; Qian et al., 2015), although only about one quarter of the mesoscale convective systems (MCSs) initiated over the Tibet Plateau during June–August 1998–2001 (Li et al., 2008) and 1998–2004 (Hu et al., 2016) can move out of the plateau with an eastward direction. Moreover, some case studies suggested the important contribution of locally triggered or intensified MCSs in the Sichuan basin to the nocturnal heavy rainfall (Ueno et al., 2011; Zhao, 2015).

A sustained heavy rainfall event occurred over the Sichuan basin during 10–18 August 2020. An 8-day accumulated rainfall amount of greater than 500 mm was distributed along the foothills on the northwestern side of the basin, with 13 rain gauge stations on the sloping mountains below 2-km height recording accumulated rainfall of greater than 1000 mm (Fig. 1). The number of rain gauge stations recording hourly rainfall rates of greater than 20 mm h^{-1} (the criterion of short-duration heavy rainfall defined by the National Meteorological Center of China (Chen et al., 2013) reached 267 (Fig. 2). The hourly rainfall rates at many stations exceeded 60 mm h^{-1}, with 13 stations exceeding 100 mm h^{-1}, and a maximum rate of 138 mm h^{-1} occurred at 1400 LST (Local Standard Time = UTC + 8 h) 11 August. The maximum daily rainfall amount reached 423 mm from 2000 LST 10 August to 2000 LST 11 August at Lushan station, which is the second highest value ever recorded in the Sichuan Province. These rainfall extremes triggered floods and geological disasters in the upper

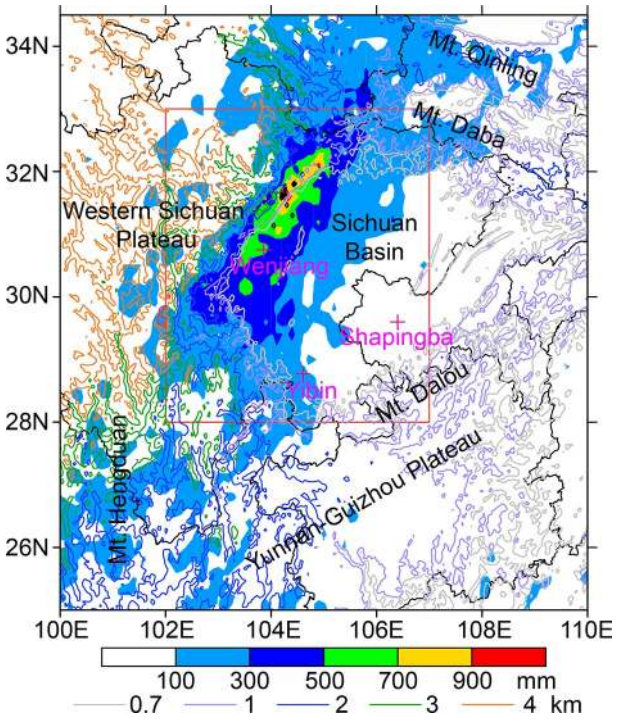

Fig. 1. The 8-day accumulated rainfall amount (shaded, mm) from 1800 LST 10 August to 1800 LST 18 August 2020, with black solid diamonds denoting stations recording rainfall greater than 1000 mm. The red rectangle denotes the target region of this study. Colored curves denote terrain heights (km). The names and locations of three sounding stations are shown by magenta crosses. The names of major mountains and other relevant locations appear in black.

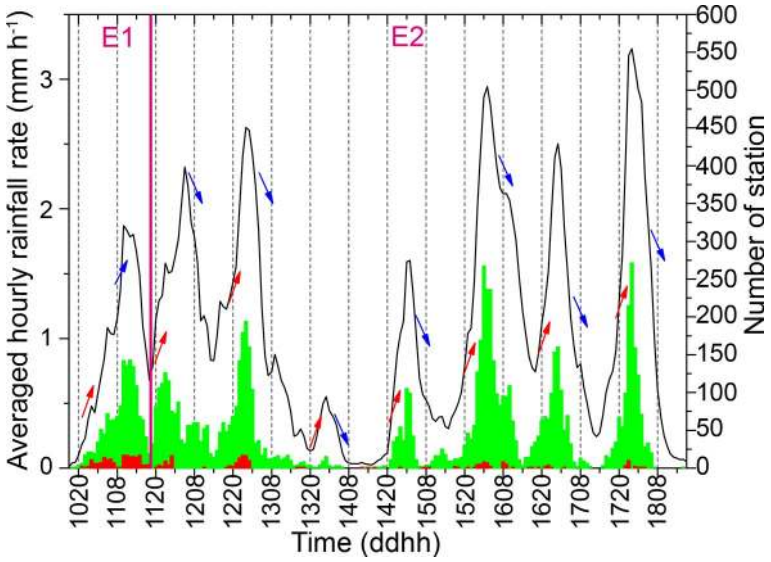

Fig. 2. Time series of the regionally averaged hourly rainfall rates (black lines) and the numbers of stations with hourly rainfall rates > 20 mm h^{-1} (green bars) and 60 mm h^{-1} (red bars), respectively, over the target region during 10–18 August 2020. There are a total of about 5400 rain gauge stations in the target region. Red and blue arrows indicate the trends of hourly rainfall rates after 2000 LST and around 0800 LST, respectively. The magenta vertical line roughly separates the rainfall episodes of E1 and E2; similarly for the remaining figures.

reaches of the Yangtze River, causing significant economic losses. The operational forecasts predicted the overall rainfall area reasonably well, but failed to accurately predict the locations and timings of heavy rainfall during the 8-day period.

Of interest is that the regionally averaged hourly rainfall rates indicated pronounced diurnal cycles with the respective maximum and minimum values occurring in the nighttime and afternoon hours during the 7-day period from 11 to 18 August, albeit having some small fluctuations (Fig. 2). The peak and minimum values occurred during 0000–0500 and 1300–1700 LST, respectively, given a 24-h cycle from 1800 to 1800 LST. These values are comparable to those found by Z19 in a 3-month composite, i.e., a peak at around 0200 LST and a minimum between 1200 and 1800 LST. However, the slight rainfall enhancement at 1400 LST between 1200 and 1800 LST found in Z19 was not evident in this case. For the sake of our subsequent discussions, we divide the entire rainfall event into two episodes: (i) from 1800 LST 10 August to 1700 LST 11 August (E1), i.e., prior to the onset of the diurnal rainfall cycles; and (ii) from 1800 LST 11 August to 1700 LST 18 August (E2). Note that the weak nighttime rainfall on 13 August is included in the E2 episode simply for the convenience of our analysis. In contrast to the E2 episode, the regionally averaged rainfall rates during the E1 episode exhibited a rising trend at around 0800 LST and started to decrease about 8 hours later.

Although numerous studies have discussed the diurnal characteristics of rainfall and associated physical mechanisms in the Sichuan basin mostly using data during a period of several months to several years, this heavy rainfall event in August 2020 provided us with an opportunity to examine to what extent this extreme rainfall case fits the previous statistical analyses. Specifically, we seek to address the following questions through this case study: Why could this heavy rainfall event persist for so long and be so extreme? How could the heavy rainfall event undergo several diurnal cycles with peak hourly rates occurring during the nighttime? Why is the evolution of hourly rainfall during the E1 and E2 episodes different? And what mesoscale processes were responsible for the nocturnal generation of heavy rainfall?

The next section describes the data and methods used in this study. Section 3 presents the synoptic patterns and their anomalies that influenced the heavy rainfall event. Section 4 examines the dominant factors that were responsible for the diurnal rainfall variations during the two episodes. Section 5 discusses the evolution of MCSs causing nocturnal rainfall enhancement and their associated environments. A summary and conclusions are given in the final section.

2. Data and methods

To examine the synoptic background, the ERA5 reanalysis (Hersbach et al., 2020) is used. The data has a horizontal grid spacing of about 31 km, and 31 vertical levels from the surface to 10 hPa with hourly intervals. The ERA5 monthly averaged data from 1981 to 2010, with the same spatial resolutions as the ERA5 hourly data, are used to meas-

ure the extent of circulation anomalies. The anomalies are standardized by dividing the difference between the average physical quantity (e.g., geopotential height) during the E2 episode and the 30-year-averaged physical quantity in August by the standard deviation of the monthly mean of August during the 30-year period. Twelve-hourly sounding observations over the target region (red rectangle in Fig. 1), obtained from the China Meteorological Administration, are used to calculate thermodynamic parameters. Black body temperature (TBB) of cloud tops from FY-2H satellite observations, provided by the National Satellite Meteorological Center of the China Meteorological Administration, are used to investigate the evolution of heavy-rain-producing convective storms.

The moisture flux across the boundary i [where i can be w (west), s (south), e (east), and n (north)] of the target region, QFlux_i, is calculated using the following equation (Zhou and Yu, 2005; Huang et al., 2019; Z19):

$$\mathrm{QFlux}_i = \frac{1}{g}\int_0^{L_i}\int_0^{P_s} qv_n \mathrm{d}p\mathrm{d}l\,,$$

where g is the gravity, L_i is the length of boundary i, P_s is surface pressure, q is specific humidity at the boundary, and v_n is the wind component normal to the boundary, which is positive inward and negative outward. This methodology has been used in Z19 to examine the mechanism of the nighttime rainfall enhancement in the Sichuan basin during three summer months of 2013. While their four boundaries are parallel to the terrain surrounding the basin, in this study a rectangular target region with its southern boundary perpendicular to the mean southerly LLJ is selected for the sake of analysis (Fig. 3b). In addition, in view of the advantages of a case study, the hourly evolution of water vapor transport across each boundary is explored and compared with the hourly rainfall evolution.

3. Synoptic-scale background and anomalies

Figure 3 shows the temporal mean circulations during the E2 episode in the middle and lower troposphere, and their anomalies with respect to a 30-year climatology. It is evident that the western Pacific subtropical high extended westward to central China with standardized anomalies greater than 4 (Figs. 3a, b), which favored persistent water vapor transport by the southerly airflow on the northwest periphery of the subtropical high to the target region. The target region was located just ahead of a distinct trough axis, albeit with weak negative anomalies, which is a favorable region for quasi-geostrophic ascent. The locations of the low-pressure trough and the subtropical high changed slightly in the daily 500-hPa circulation fields (not shown). The relatively north or west position of the trough axes affected the strength and path of cold air, which in turn impacted the appearance and distribution of cold fronts. As shown in Fig. 4, a cold front extended from northeast China southwestward to the target region on 16 and 17 August, with another cold front to the southeast of the target region on 12 August. At 800 hPa (Fig. 3b), we can see an abnormally strong monsoon trough over the Bay of Bengal and another distinct trough over the Indochina Peninsula, both favoring the northeastward transport of water vapor to southwest China. In addition, the region of high-pressure gradients to the southeast of the target region indicates the presence of a southerly LLJ transporting moist, warm air into the target region. The target region exhibited a center of lower pressure at 800 hPa, with strong negative anomalies > 3, which was associated with presence of the southwest vortices; and coinciding with the vortices was a weak warm core.

The abovementioned synoptic pattern led to ample moisture over the target region during E2 (Fig. 3c). The 7-day averaged precipitable water exceeded 60 mm over the Sichuan basin but was much smaller outside, implying that the total atmospheric column over the basin was much moister than its surrounding regions. The standardized anomalies over the northwest of the basin reached 3–4, which is consistent with the accumulated rainfall center (cf. Figs. 1 and 3c). The distribution of specific humidity at 800 hPa (Fig. 3d) shows high values of ~ 14.5 g kg^{-1} and anomalies > 2–3 in and to the south of the target region that are accompanied by anomalous southerly moisture flux, implying strong water vapor transport from the south. Surface maps (Fig. 4) also show that near-surface specific humidity over the target region reached 15 g kg^{-1} at 2000 LST every day from 10 to 17 August 2020.

For the purpose of comparison, a surface map during the E1 episode is given in Fig. 4a showing that the western Pacific subtropical high was located more to the east at 2000 LST 10 August, as indicated by the 1005-hPa isobar, partly due to the influence of Typhoon Mekkha la (2020). This was not conducive to the development of an LLJ to the southeast of the target region. The weather systems favoring heavy rainfall production during the E1 episode included a low-pressure trough associated with a Tibetan vortex to the west of the target region at 500 hPa (not shown) and a southwest vortex in the lower troposphere over the basin (Fig. 4a)

4. Dominant processes controlling the diurnal rainfall cycles

4.1. *Spatial distributions of rainfall and low-level flows*

Before analyzing the dominant processes controlling the diurnal rainfall cycles, especially the nocturnal rainfall enhancement, we examine the evolution of the total 3-hour accumulated rainfall amounts during the E2 episode (Fig. 5). A major rainfall belt > 50 mm was distributed in the northwestern corner during the early evening hours (i.e., 1800 to 2000 LST, Fig. 5a). The rainfall belt weakened slightly in intensity in the following three hours, while another major rainfall belt developed in the southwestern area of the basin, which was more extensive in coverage, and a secondary rain-

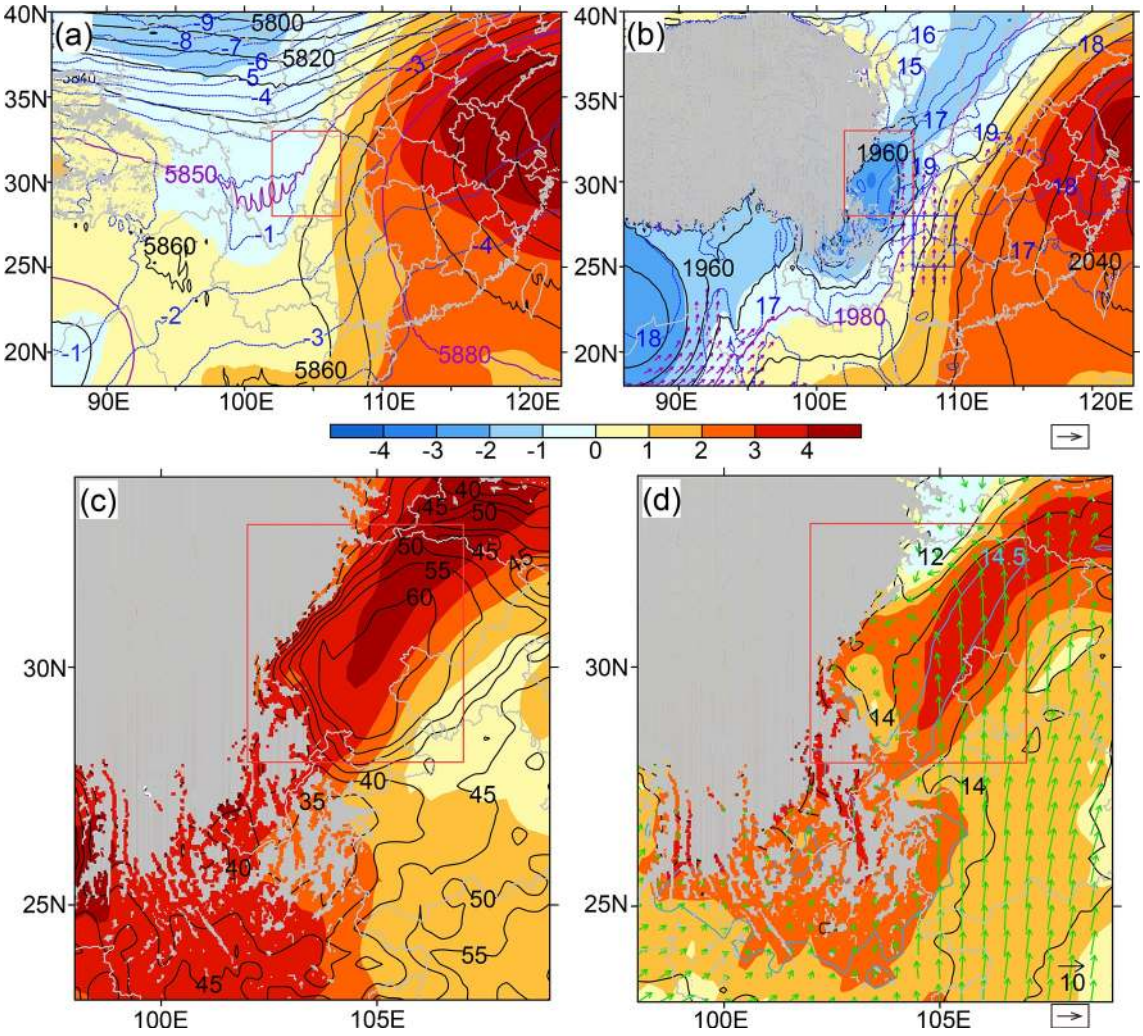

Fig. 3. Distribution of the averaged (a) 500-hPa and (b) 800-hPa geopotential heights (contoured at 10-gpm intervals) and isotherms (contoured at 1°C intervals), (c) precipitable water (contoured at 5-cm intervals), and (d) 800-hPa specific humidity (contoured at 1 g kg^{-1} intervals) during the E2 episode. Standardized anomalies with respect to the 30-year mean quantity of the months of August from 1981 to 2010 are shaded. Purple arrows in (b) show the mean horizontal wind > 10 m s^{-1} at 800 hPa. Green arrows in (d) show the moisture flux anomalies at 800 hPa (g s^{-1} cm^{-1} hPa^{-1}). The contours of 5850, 5880 and 1980 gpm are highlighted in purple in (a) and (b). Blue contours in (d) denote specific humidity of 14.5 g kg^{-1}. Gray shading represents terrain higher than (a) 5 km and (b, c, d) 2 km. The red rectangles indicate the target region of this study. The blue rectangle in (b) is used in Fig. 10.

fall belt appeared in the central region, as highlighted by the two ellipses in Fig. 5b. This corresponded to rapid increase in the regionally averaged hourly rainfall rates during the diurnal cycle (cf. Figs. 5b and 2). The enhancement of 6-hourly rainfall over the southwestern basin from 2000 to 0200 LST was evident during each day from 11 to 17 August except for 13 August (not shown). At the time of the peak regionally averaged hourly rainfall rate (i.e., 0000–0200 LST), the 3-hourly rainfall totals exhibited a widespread coverage, with heavier amounts of over 150 mm in both the northwestern and western basins (Fig. 5c). Subsequently, heavy rainfall was approximately linearly distributed along the foothills on the northwestern side of the basin. The nighttime rainfall was first enhanced over the southwest part of the basin, which then extended to the northwest. This evolution is consistent with that shown in Z19. The rainfall intensity and areal coverage decreased gradually after about 0200 LST. While the 3-hourly heavy rainfall belt in the southwestern basin occurred during the nocturnal period, it did not show up in the 8-day accumulated rainfall map (cf. Figs. 5b, c and 1), because of the more frequent development of rainstorms in the northwestern basin.

Figure 6 shows that the convergence pattern at 800 hPa coincided well with the diurnal evolution of the rainfall distribution. For example, the convergent wind belt $< -4 \times 10^{-5}$ s^{-1} sustained over the northwest of the basin, which is consistent with the 8-day accumulated rainfall distribution (Fig. 1). Of course, this is not surprising because the convergence zone could be understood to result from diabatic heating associated with these storms. The wind convergence over the

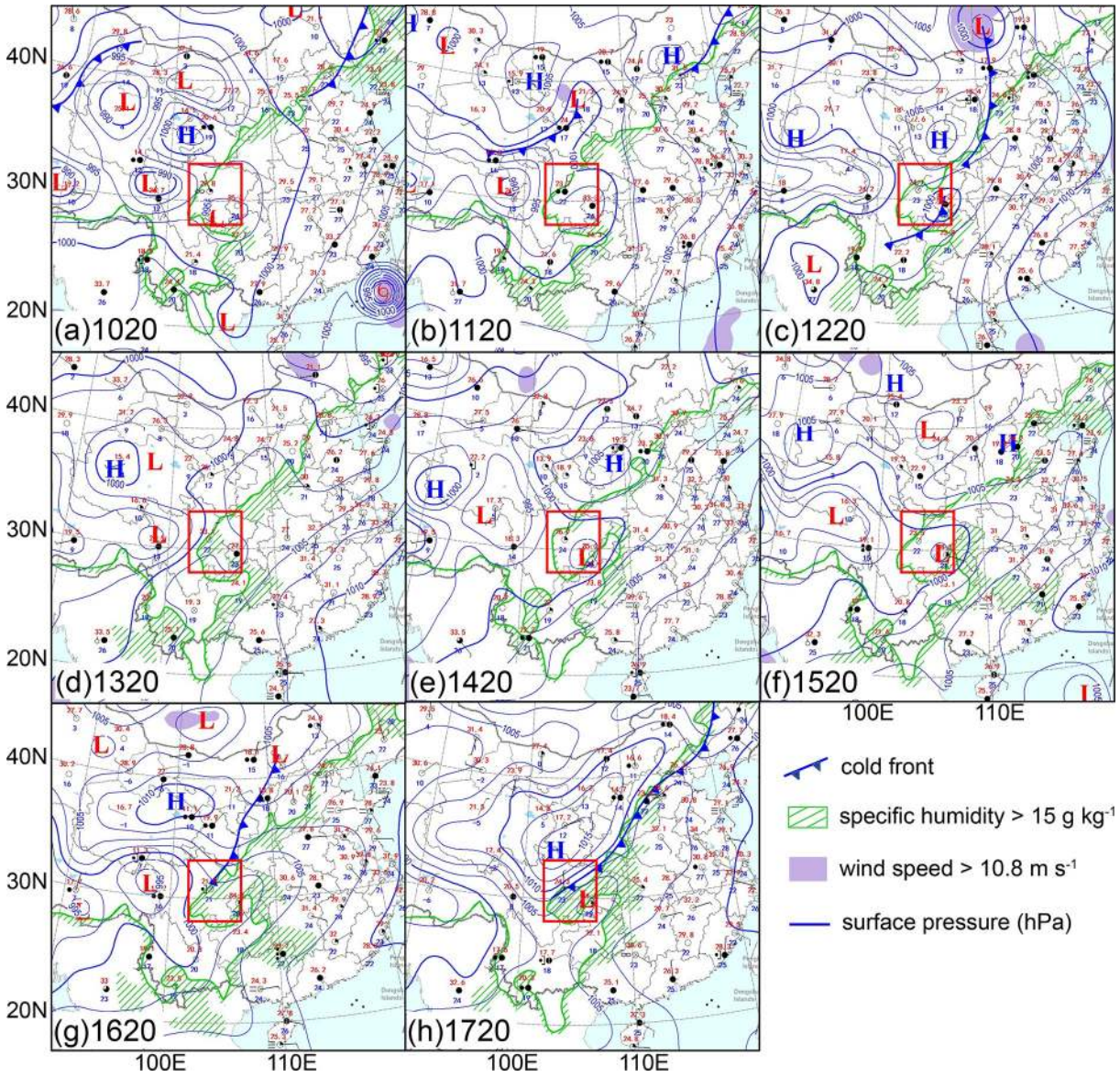

Fig. 4. Daily surface maps at 2000 LST from 10–17 August obtained from the National Meteorological Center of China Meteorological Administration. Time in form of ddhh (LST) is shown in the left-bottom corners. The red rectangles denote the target region of this study.

southwestern part of the basin intensified during 2100–2300 LST due to the presence of relatively stronger easterly winds from the southeast, which is in accordance with the rainfall enhancement in the southwestern part of the basin (Figs. 5a, b and 6a, b). Deviating winds distributed close to the northwestern mountains north of 31°N changed from northeasterly at 1800–2000 LST to southeasterly at 0000–0200 LST, which enhanced the convergence and thus intensified the rainfall over the northwest part of the basin (Figs. 5a, c and 6a, c).When the deviating winds near 104°E in the south of the basin changed from the southeasterly to southerly direction during 0000 to 0500 LST, the convergence and the rainfall over the southwest part of the basin weakened greatly (cf. Figs. 5c, d and 6c, d). During the daytime, a convergence zone always maintained over the northwestern part of the basin, with a slight northeastward displacement of its center in the afternoon, which is in accordance with the heavy rainfall distribution over that region (Figs. 5e–h and 6e–h). All the results indicate that the diurnal variation of the low-level wind field was closely related to that of rainfall distribution in the target region.

The nocturnal enhancement of rainfall was also related to the low-level thermal field. As indicated by pseudo-equivalent potential temperature (θ_{ep}, Figs. 6a–c), there was an obvious contrast of θ_{ep} between an airflow along the foot of the plateau to the west and an airflow extending northward from the southern target region during the evening to early morning hours. The difference in θ_{ep} at 2100–2300 LST reached about 12 K in a distance of about 200 km. A high θ_{ep} tongue > 354 K was associated with a southerly LLJ, while an extended narrow zone with a 100–150 km width next to the western plateau was associated with a colder air-

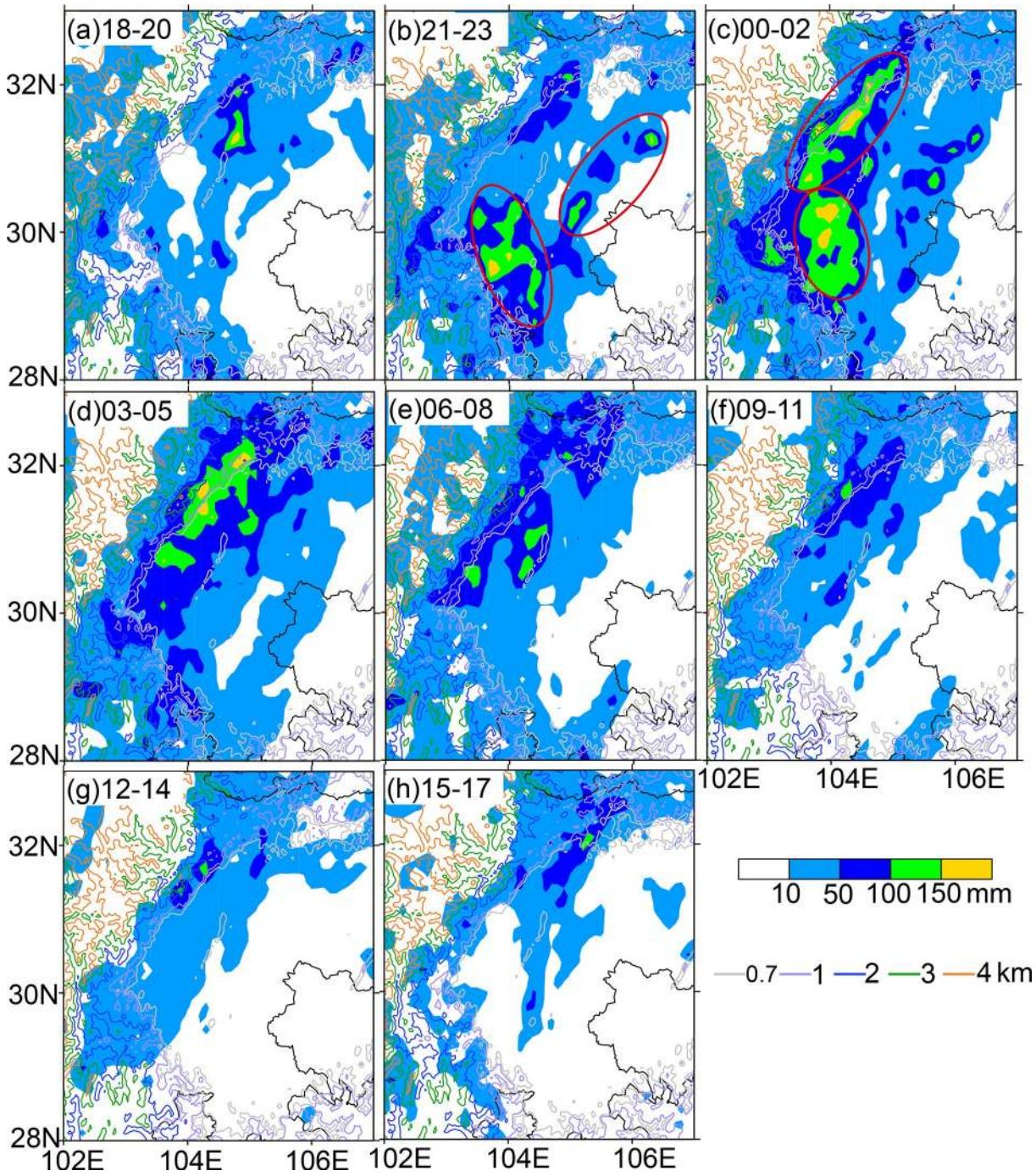

Fig. 5. The total 3-hourly accumulated rainfall (mm) during the E2 episode. Time period in the form of hh–hh (LST) is shown in the upper-left corners in each panel. Curves denote terrain heights (km). Red ellipses denote the regions with 3-hourly rainfall amounts exceeding that in the previous 3 hours.

mass probably due to rain evaporative cooling (cf. Figs. 5a, b and 6a, b). This thermal contrast was conducive to convective initiation in the southwestern part of the target region during the evening hours. This will be further discussed in section 5.

The diurnal cycles of heavy rainfall in the basin coincided closely with the development of the southwest vortices. Figure 7 shows that the mean relative vorticity in the Sichuan basin was $< 6 \times 10^{-5}$ s^{-1} during the E1 episode, but was substantially larger during E2. The vorticity peaked in the 850–800 hPa layer during the early morning hours each day of the E2 episode, with the maximum value being $> 10^{-4}$ s^{-1} except for the much weaker rainfall period of 13 August. The timings of the peak vorticity coincided well with those of the peak rainfall rate, suggesting the importance of latent heat release in the generation and intensification of the southwest vortices, which in turn favored upward motion and heavy rainfall production (e.g., Zhang and

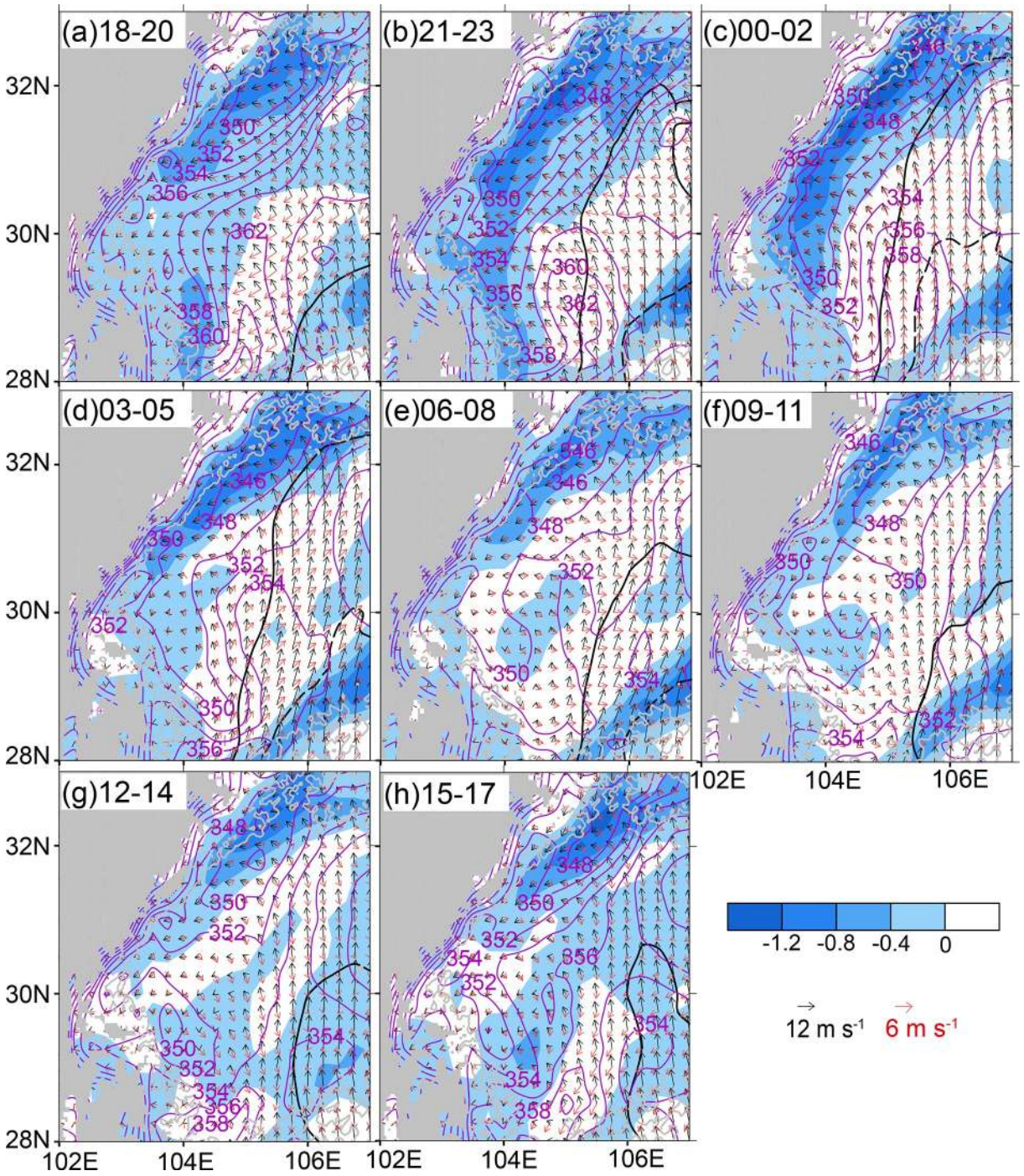

Fig. 6. Three-hourly averaged 800-hPa wind (black vectors) and its deviation (red vectors) and divergence (blue shading, 10^{-4} s^{-1}), and 900-hPa θ_{ep} (purple-contoured at 2-K intervals) during the E2 episode. Time period in the form of hh–hh (LST) is shown in the upper-left corner in each panel. Isotachs of 10 and 14 m s^{-1} are shown by solid and dashed black contours, respectively. Gray shading and curved lines represent terrain higher than 2 km and terrain of 1 km elevation, respectively. Note the θ_{ep} over the region with terrain height of greater than 1 km are fake.

Fritsch, 1987; Kuo et al., 1988; Li et al., 2014). Such positive feedbacks among latent heat release, increased rotation, and increased low-level convergence associated with the southwest vortices could explain the nocturnal enhancement of rainfall over the basin, with the southerly LLJ feeding the needed high-θ_{ep} air, as discussed in the next subsection.

4.2. *LLJ and water vapor fluxes*

Given the importance of the southerly airflow to the southeast of the basin in transporting water vapor to the basin (Figs. 3b, d), how the lower-tropospheric flows varied diurnally in and around the basin was examined. The 3-hourly averaged wind fields during E2 (Fig. 6) show that a

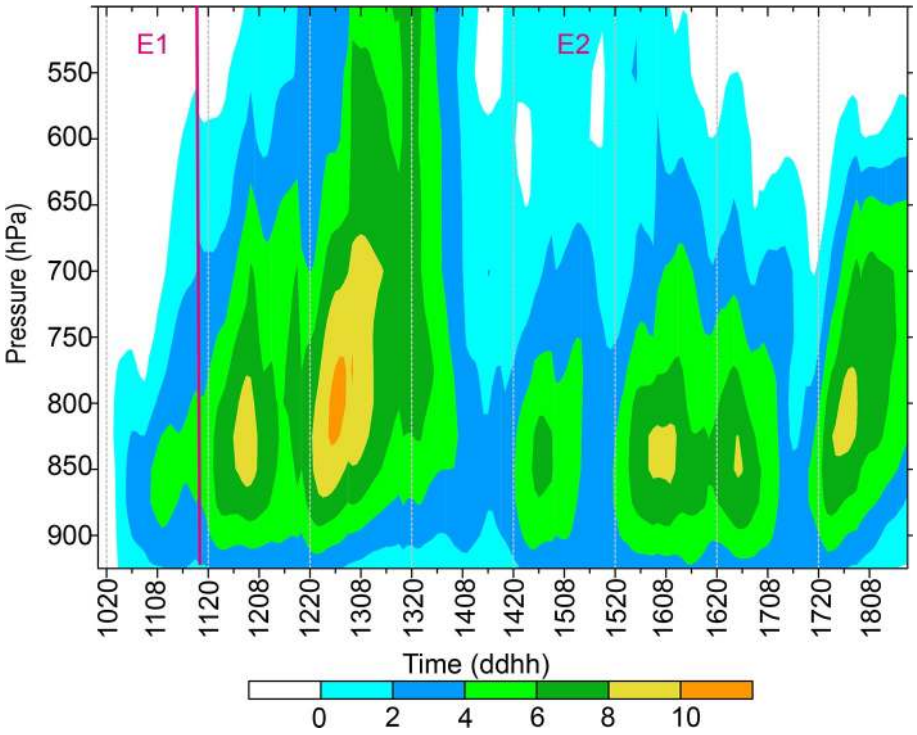

Fig. 7. Time series of the vertical distribution of relative vorticity (10^{-5} s^{-1}) averaged over the target region with terrain elevations of less than 700 m.

southerly LLJ was located in the eastern part of the target region, with its coverage and intensity increasing during the late evening to early morning hours and decreasing during the daytime, as indicated by the isotachs of 10 and 14 m s^{-1}. Meanwhile, the direction of the LLJ varied from southeasterly in the evening to southerly near midnight, and then to southwesterly in the morning hours. As a result, deviating winds rotated in a clockwise sense. These variations in wind direction and speed, based on the 7-day composite, were similar to those found by Z19 based on their three-month composites. Given the topographical features to the east of the target region, we may infer that the deviating winds helped enhance water vapor transport into the target region when they were close to the eastern and southern boundaries of the target area with some components crossing the boundaries. For example, the deviating winds to the southeast of the basin exhibited easterly, southeasterly, southerly, and southwesterly directions chronologically during the evening to early morning hours, which would increase the water vapor transport and result in rainfall enhancement during about 2100 to 0500 LST (Figs. 6b–d). In contrast, the deviating winds with a westerly, northwesterly or northerly direction during daytime would reduce the transport of water vapor. This conjecture is confirmed by an analysis of moisture flux across the four boundaries of the target region.

Figures 8a–d show that the southern boundary was the main channel for water vapor transport into the basin during E2, followed by the eastern and western boundaries. The largest water vapor flux of greater than 16 g s^{-1} cm^{-1} hPa^{-1} was at ~ 800 hPa across the eastern portion of the southern border, which is consistent with the location of the southerly LLJ. At the eastern boundary, the largest water vapor flux > 8 g s^{-1} cm^{-1} hPa^{-1} was distributed at ~ 900 hPa, which is associated with the lower terrain height there. Water vapor was advected out mainly from the northern boundary, and also from the eastern boundary above the PBL.

The temporal variations of the moisture flux through the four boundaries (Fig. 8e) indicate that the water vapor flux across the southern boundary ($QFlux_s$) had evident diurnal cycles during E2, with a peak occurring close to the time of the target-region-averaged hourly rainfall rates (Fig. 2). $QFlux_s$ generally peaked when the deviating winds had their largest northward component at 800 hPa (cf. Figs. 6c and 8e). It seems that the net moisture flux through the four boundaries evolved consistently with the regionally averaged rainfall intensity (cf. Figs. 2 and 8f), e.g., the lowest peak value of net moisture flux during the evening of 13 August was consistent with the lowest rainfall peak value on the same day. The peak hour of the net moisture flux was roughly 1–6 hours earlier than the peak hour of the regionally averaged hourly rainfall, which is comparable to the 4-hour time difference found in Z19. This result confirms that the rainfall intensity in the basin was closely related to the amount of external water vapor supply (cf. Figs. 2 and 8f). In contrast to the E2 episode, there was water vapor transport with comparable strength from three boundaries during the E1 episode, i.e., the western, southern and eastern

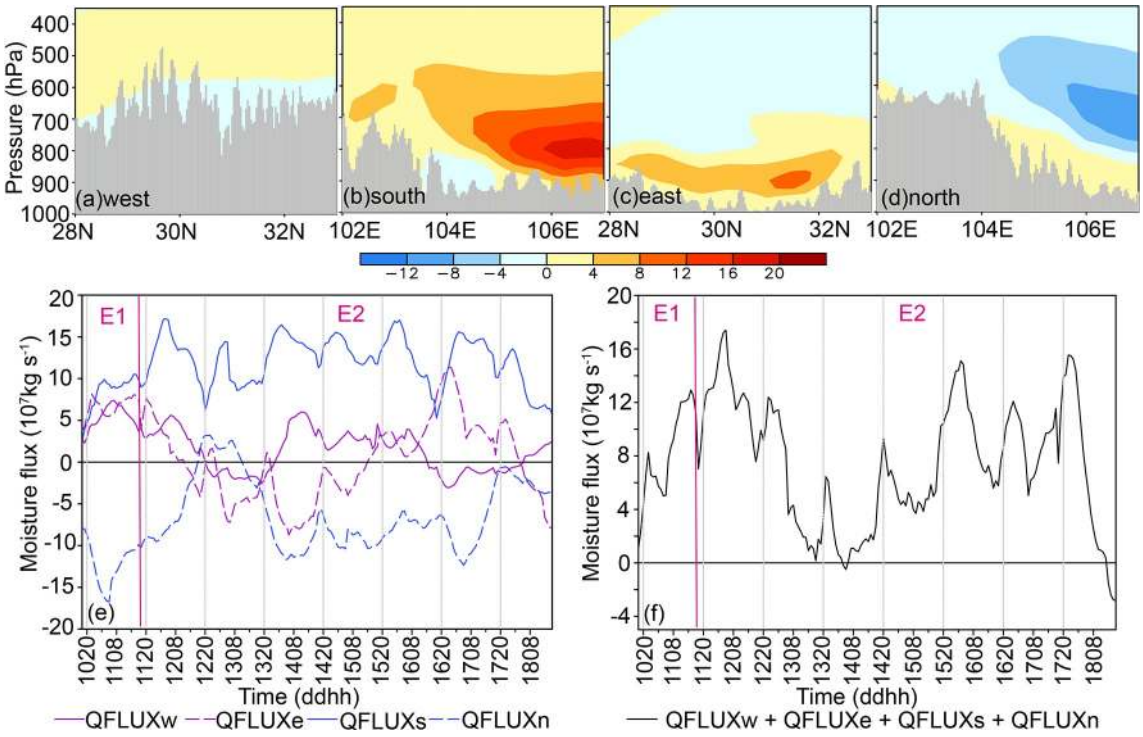

Fig. 8. Vertical cross sections of the averaged moisture flux (g s^{-1} cm^{-1} hPa^{-1}) during the E2 episode across the (a) western, (b) southern, (c) eastern, and (d) northern boundaries of the target region shown in Fig. 1. Gray shadings represent terrain. Time series are shown of (e) the averaged moisture flux across each boundary (10^7 kg s^{-1}), and (f) the net moisture flux through the four boundaries (10^7 kg s^{-1}) from 10 to 18 August 2020.

boundaries, resulting in strong net water vapor inflow, especially during the daytime. This was in accordance with the long-lasting heavy rainfall till the daytime during E1.

4.3. *Mechanisms governing the nocturnal LLJ enhancement*

The time-latitude distribution of the 800-hPa flow over the LLJ region clearly shows the diurnal evolution of the southerly LLJ during E2 (Fig. 9). Clearly, the zonally averaged horizontal wind speed increased to > 14 m s^{-1} at nighttime and decreased to < 12 m s^{-1} in the daytime during E2. Accordingly, the associated deviating wind speeds exhibited similar changes. In addition, the deviating winds presented periodic clockwise rotation and oscillation during each 24-h cycle of E2. Such oscillations of the deviating winds could enhance the water vapor convergence at nighttime, as shown previously. In contrast to the E2 episode, the zonally averaged wind speed during E1 was much smaller, i.e., 6–10 m s^{-1}, and the deviating winds were mainly northeasterly over the eastern target region, which was more or less related to the distribution of large-scale pressure systems (Fig. 4a).

The periodic variation of the deviating wind field over the LLJ region during E2 was evidently related to the inertial oscillation of the ageostrophic wind component, as previously put forward by Z19. The inertial oscillation period is $2\pi/f$, where f is the Coriolis parameter (Blackadar, 1957; Markowski and Richardson, 2010). Thus, the ageostrophic wind component would take about 24 h to rotate clockwise in a circle at 30°N, which is consistent with the duration of one cycle in this event. The wind averaged over the LLJ region to the southeast of the target region was supergeostrophic when it peaked at nighttime and subgeostrophic when it reached a minimum during the daytime (Fig. 10), which is in line with the theory of inertial oscillation. However, it is not possible to identify this phenomenon in the LLJ region to the east of the target region, because of the presence of complex terrain, as well as the likely presence of gradient wind induced by the southwest vortices.

The periodic variation of the LLJ could also be influenced by the terrain thermal forcing (Holton, 1967) as the southerly LLJ was located over the eastern part of the Yunnan-Guizhou Plateau (Figs. 1 and 3b). To minimize the influence of the southwest vortices over the basin, a zonal cross section to the south of the target region is given in Fig. 11, showing the presence of a significant mountain-plains solenoid. There were easterly deviation winds in the near-surface layer, and upward (downward) motion over the western high mountains (eastern lower mountains) at 1400 and 2000 LST (Figs. 11a, b). In contrast, the deviation circulation in the cross section was reversed at 0200 and 0800 LST (Figs. 11c, d), and was closely related to the temperature gradient of opposite sign over the sloping terrain. The easterly deviation wind at 2000 LST was stronger than that in the afternoon. Under the influence of the Coriolis force, a southerly wind could be produced in a few hours, which would help the strengthening of the LLJ during the night-

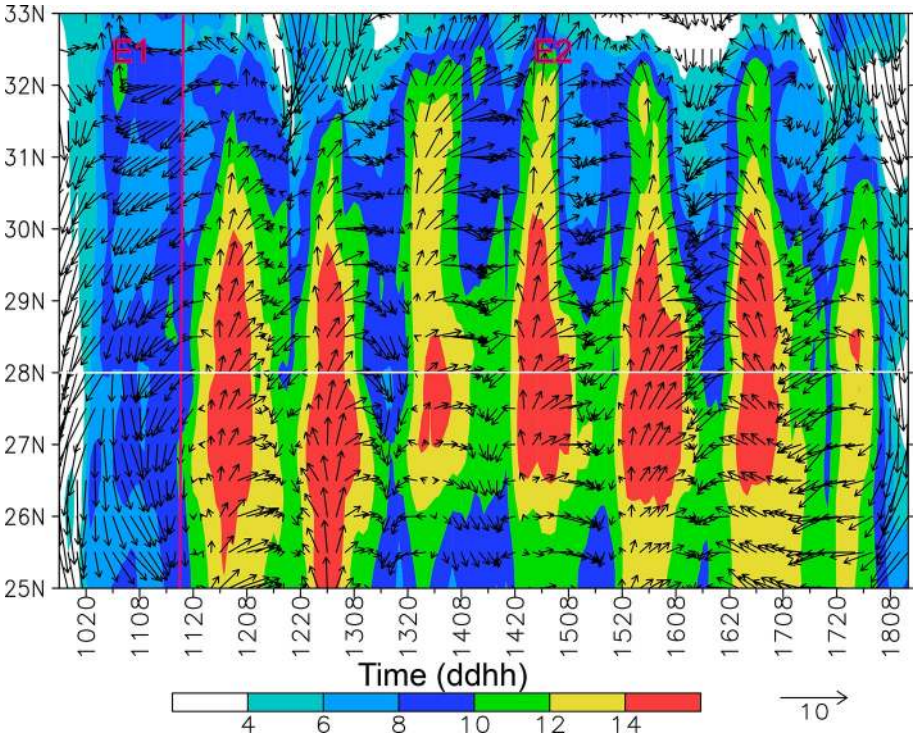

Fig. 9. Time series of the horizontal wind speed at 800 hPa (shaded, m s^{-1}) averaged over 105°–108°E during 10 to 18 August 2020. Deviations from the temporal means during E2 are shown as vectors (m s^{-1}). The white line denotes the southern border of the target region.

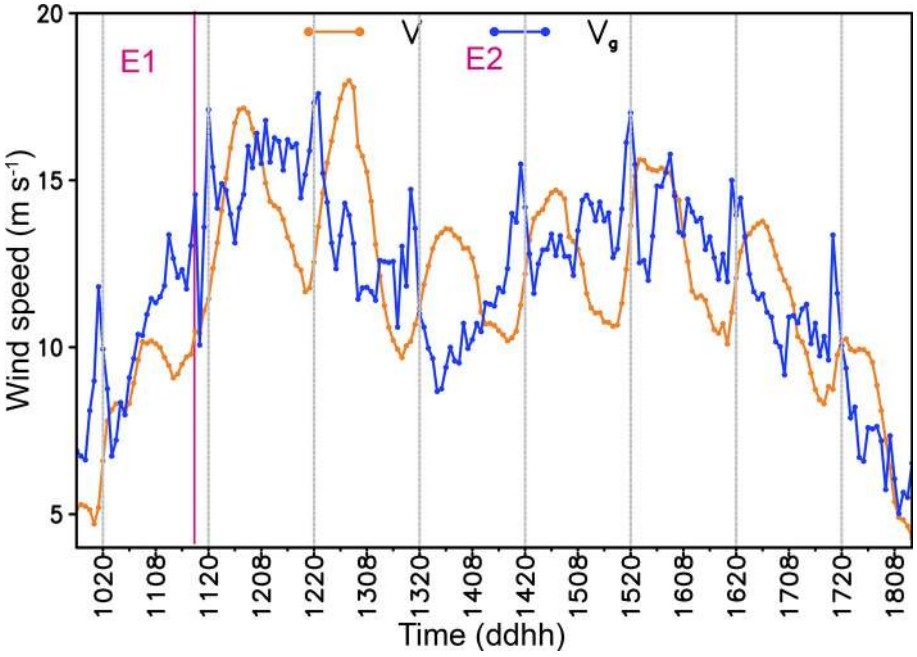

Fig. 10. Time series of area-averaged (25°–28°N, 107°–110°E; see the location in Fig. 3b) geostrophic wind speed (V_g, m s^{-1}) and horizontal wind speed (V, ms^{-1}) at 1 km above the ground.

time. Therefore, the periodic variation of the southerly LLJ could be attributed primarily to the inertial oscillation and secondarily to terrain thermal forcing (Du and Rotunno, 2014; Shapiro et al., 2016).

5. Mesoscale processes associated with the nocturnal rainfall enhancement

Figure 12 shows that convective clouds were initiated

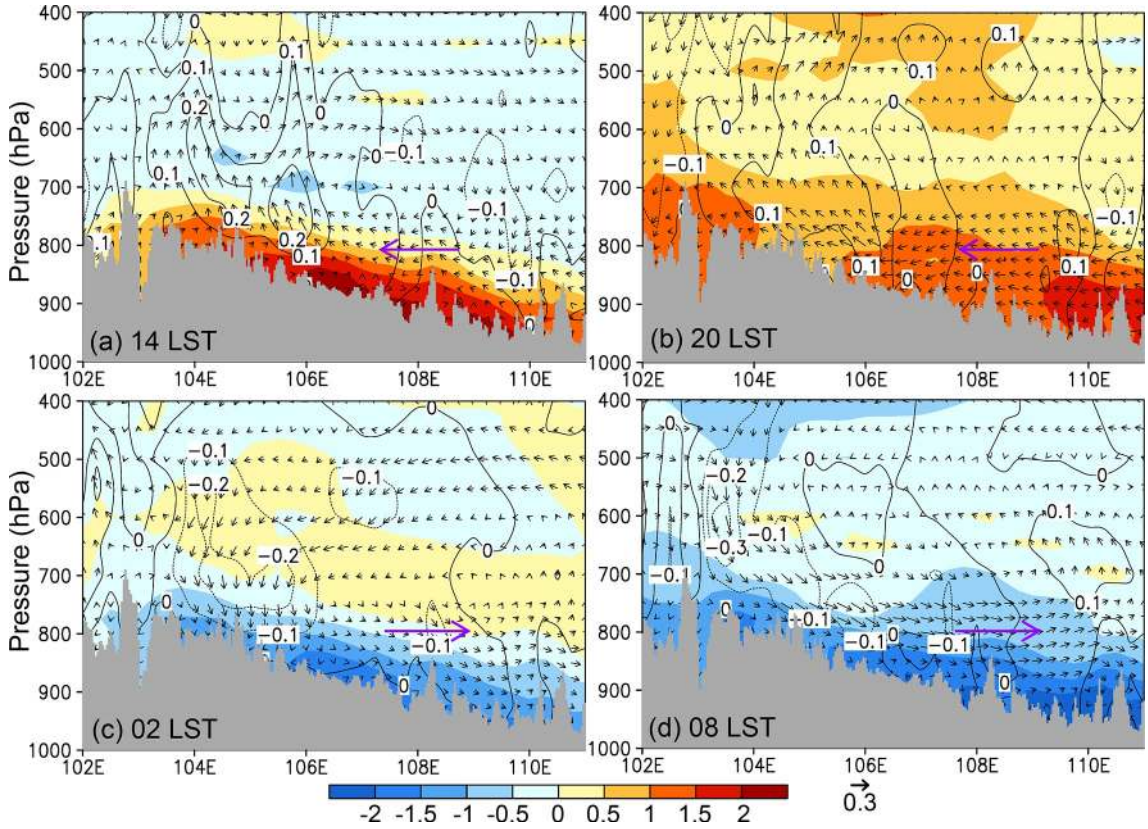

Fig. 11. Zonal cross sections of the deviation temperature (shaded, K), deviation wind [composite of zonal wind (m s^{-1}) and vertical wind (cm s^{-1})], and deviation vertical velocity (contour, cm s^{-1}) averaged between 26.5°–27.5°N at (a) 1400, (b) 2000, (c) 0200, and (d) 0800 LST during the E2 episode. Gray shadings denote terrain along 26.5°N.

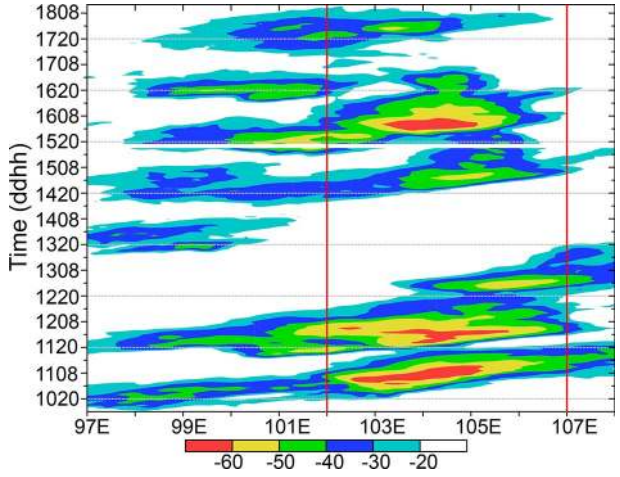

Fig. 12. Time series of the meridionally averaged TBB (°C) between 28°N and 33°N from 10 to 18 August 2020. The two vertical red lines indicate the western and eastern boundaries of the target region.

over the plateau to the west of the target region during the afternoons from 10 to 18 August (except on 12 August) 2020, with an eastward movement west of 102°E. This region is one of the two regions where MCSs are the most frequently initiated in summer over the Tibetan Plateau (Li et al., 2008; Sugimoto and Ueno, 2010; Hu et al., 2016). The convection initiation was typically correlated with the potential instability in the afternoon over the high mountains, as depicted in many previous studies (e.g., Li et al., 2008; Bao et al., 2011; Xia et al., 2015; Qian et al., 2015). The eastward extension of the convective clouds was obvious on some days, e.g., during 2000 LST 10 August to 0800 LST 11 August, and during 2000 LST 14 August to 0200 LST 15 August. Their eastward movement to the west of the target region suggests a relationship between the convection over the western plateau and the convective clouds in the basin, as noticed in previous studies (Wang et al., 2005; Bao et al., 2011; Qian et al., 2015). The convective clouds over the basin had lower cloud-top TBB than those over the high plateau to the west (Fig. 12), due to the more abundant moisture and stronger dynamic lifting over the basin associated with the LLJ.

The evolution of MCSs leading to the nocturnal rainfall enhancement over the basin can be seen from the hourly variation of the cloud-top TBB around the target region (Fig. 13). It is apparent that convective clouds were initiated over the southwest basin mostly during the evening hours (Figs. 14b, e, n, q, t, w), and grew stronger in a few hours, producing heavier rainfall during the nighttime, except on 12 and 13 August (Figs. 14h, k). On the evening of 12 August, three convective cells were oriented from southwest to northeast over the target region (Fig. 13h), where convection previously existed in the late afternoon (Fig. 13g).

During the evening of 13 August, convective clouds with TBB < −30 were absent in the target region, which was in accordance with the weak rainfall intensity during the same period (cf. Figs. 13j–l and 2). It seems that the convection

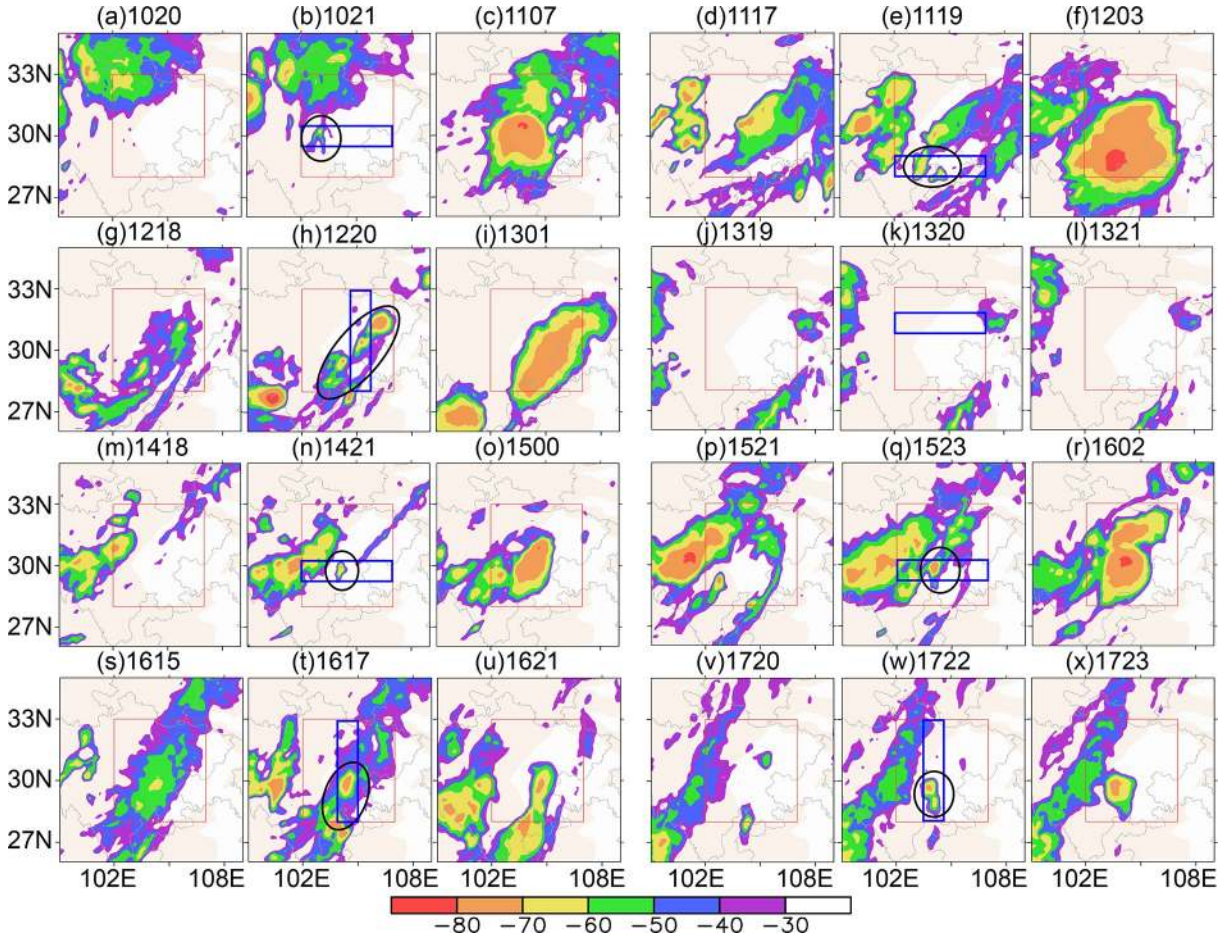

Fig. 13. Distribution of TBB (°C) at selected times. Time in the form of ddhh (LST) is shown above each panel. Three times were selected for each daily cycle, representing the time immediately before the convection in the target region was triggered or strengthened, when it was triggered or strengthened, and when the cloud was the deepest during its lifetime. The solid ellipses denote the positions of newly initiated convection. Light beige shadings represent terrain above 1 km. The blue rectangles in the second and fifth columns are used to plot the cross sections shown in Fig. 15. The red rectangles denote the target region of this study.

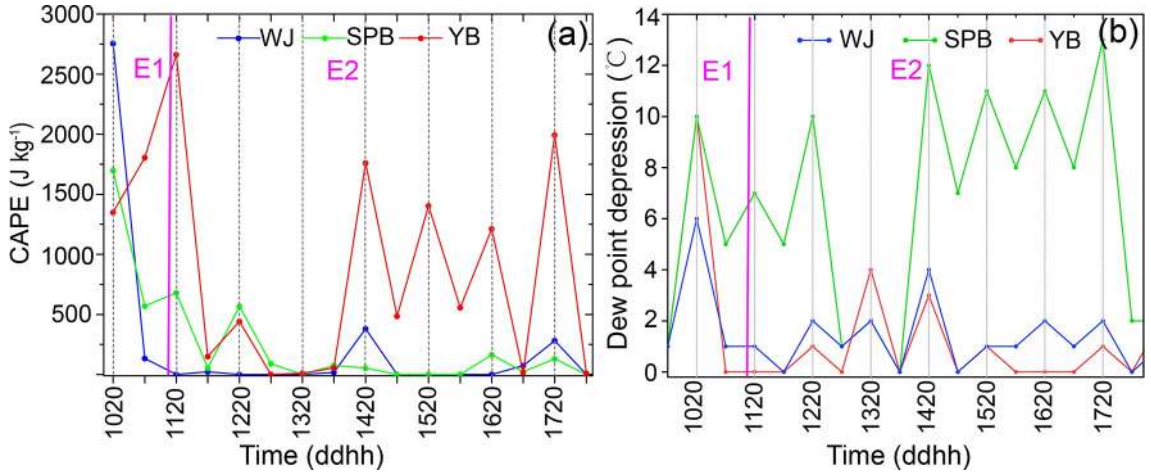

Fig. 14. Time series of the (a) convective available potential energy (CAPE, J kg^{-1}) and (b) surface dew-point depression over the Wenjiang, Shapingba and Yibin sounding stations (see their locations in Fig. 1).

propagating from the western Sichuan Plateau made limited contribution to the enhancement of rainfall in the target region during the evening hours, as only a small fraction of the convective clouds entered the target region during the event. Moreover, some of them rapidly weakened when they moved close to the basin or merged with the precipitation systems in the basin (Figs. 13b–c, e–f, n–o, q–r, w–x).

To gain further insight into the convective initiation in the southwestern basin during the evening hours, the convective available potential energy (CAPE) and surface dew-point depression at three sounding stations in the target region (magenta crosses in Fig. 1) are compared in Figs. 14a, b. The CAPE at Yibin station (located in the southern target region) started increasing at 2000 LST every day during the E2 episode, with the maximum value of 2662 J kg^{-1} on 11 August (Fig. 14a). In contrast, the Wenjiang and Shapingba stations (located in the western and southeastern target regions, respectively) had much smaller CAPE values than that at Yibin station, although they also exhibited an increase in CAPE at 2000 LST relative to 0800 LST on a few days. Moreover, the near-surface air at the southern and western stations was moister than that at the eastern station, as indicated by the dew-point depressions (Fig. 14b). This explains partly why the convection was mainly initiated in the southwestern target region during the evening hours.

Cross sections through the initiated or intensified convective clouds are shown in Fig. 15 in order to examine the mechanisms of convection development during the evening hours of E1 and E2. Generally, the development of convection during E2 can be classified into two categories. In the first category, a cold front appeared in the basin (Figs. 4c, g, h), as indicated by the dense and slantwise θ_{ep} surfaces (Figs. 15c, g, h). The associated cold air advection can be seen clearly from the northerly downslope winds in the northern target region (Figs. 15c, g, h). To the south of the slantwise θ_{ep} surface, high-θ_{ep} air > 372 K (Fig. 15c) and 356K (Fig. 15h) was conditionally unstable and extended upward from the surface at 2000 LST 12 and 2200 LST 17 August, respectively. At 1700 LST 16 August (Fig. 15g), the lowest 100 hPa layer south of 29°N was conditionally stable probably due to rain evaporative cooling in that region (Figs. 13s, t). However, vertical columns to the east of the 105°E were conditionally unstable, with θ_{ep} > 364 K (not shown). It is the slantwise lifting of the high-θ_{ep} air above the cold front, and the release of convective instability, that accounted for the initiation or intensification of convection in the basin. In addition, the southwest vortex with relative vorticity of greater than 10^{-4} s^{-1} in the lower troposphere could be enhanced by latent heating, which would in turn enhance the low-level wind convergence and ascent.

In the second category, neutral to stable vertical columns with relatively colder air to the west were present close to the western Sichuan Plateau during the evening hours of 11, 14, and 15 August (Figs. 15b, e, f). This was probably associated with rain-evaporation cooling induced by the daytime convection propagating eastward from the western plateau, especially on 14 and 15 August (cf. Figs. 15e, f and 13n, q). The rain evaporative cooling, sometimes manifested as a strong cold pool, could interact with high-θ_{ep} air inflow leading to convection initiation (Wu and Luo, 2016; Tu et al., 2017; Liu et al., 2018; Zhang et al., 2018). The southerly warm, moist airflow into the target region was conditionally unstable with high θ_{ep} of 368–376K, and ascended over the colder air (Figs. 15b, e, f). In contrast, the airflow across the eastern boundary was mainly below 850 hPa, with a lower center of moisture flux (Fig. 8c). This airflow was uplifted over the region where the southwest vortices were located, and ascended in a slantwise sense to meet the southerly airflow at 800 hPa. The ascending airflow over the relatively colder layer was important for convective initiation and the release of conditional instability. For the sake of completeness, Fig. 15d shows the vertical circulation in the evening of 13 August when the weakest rainfall during E2. The eastern portion of the basin appeared to be marginally convective unstable, which was consistent with the development of cloud cluster there.

In the evening of 10 August during E1, the basin exhibited a much wider region of warm, moist air than that during the evenings of the E2 episode. The presence of high θ_{ep} air > 372 K between 104°E and 107°E was consistent with the high CAPE at the three sounding stations (cf. Figs. 14a and 15a). With the lower-tropospheric easterly winds approaching the plateau and the wind convergence over the mountain slopes (Fig. 15a), the release of conditional instability benefited from the terrain lifting of the high θ_{ep} air, resulting in the convection initiation in the southeastern basin. Moreover, quasi-geostrophic lifting ahead of the mid-tropospheric trough axis associated with the Tibetan vortex should also play an important role in E1.

6. Summary and conclusions

In this study, we examined a sustained heavy rainfall event that occurred over the Sichuan basin in southwest China during 10–18 August 2020, with accumulated rainfall > 1000 mm over the northwestern part of the basin, and a maximum hourly rainfall rate of 138 mm h^{-1}. The regionally averaged hourly rainfall exhibited a pronounced diurnal cycle on most days, with respective peak and valley values mostly occurring in the night and afternoon. The maximum accumulated rainfall during the event was located over the northwestern part of the basin, mainly due to the cumulative effect of the frequent heavy rainfall there with a nocturnal peak rainfall amount. The rainfall over the southwest of the basin was also enhanced at night, despite smaller rainfall accumulation owing to the relatively shorter rainfall duration.

The persistence of heavy rainfall during the E2 episode (from 1800 LST 11 August to 1700 LST 18 August) was mainly attributed to the quasi-stationary position of the western Pacific subtropical high and the presence of a westerly midlevel trough to the west or northwest of the target

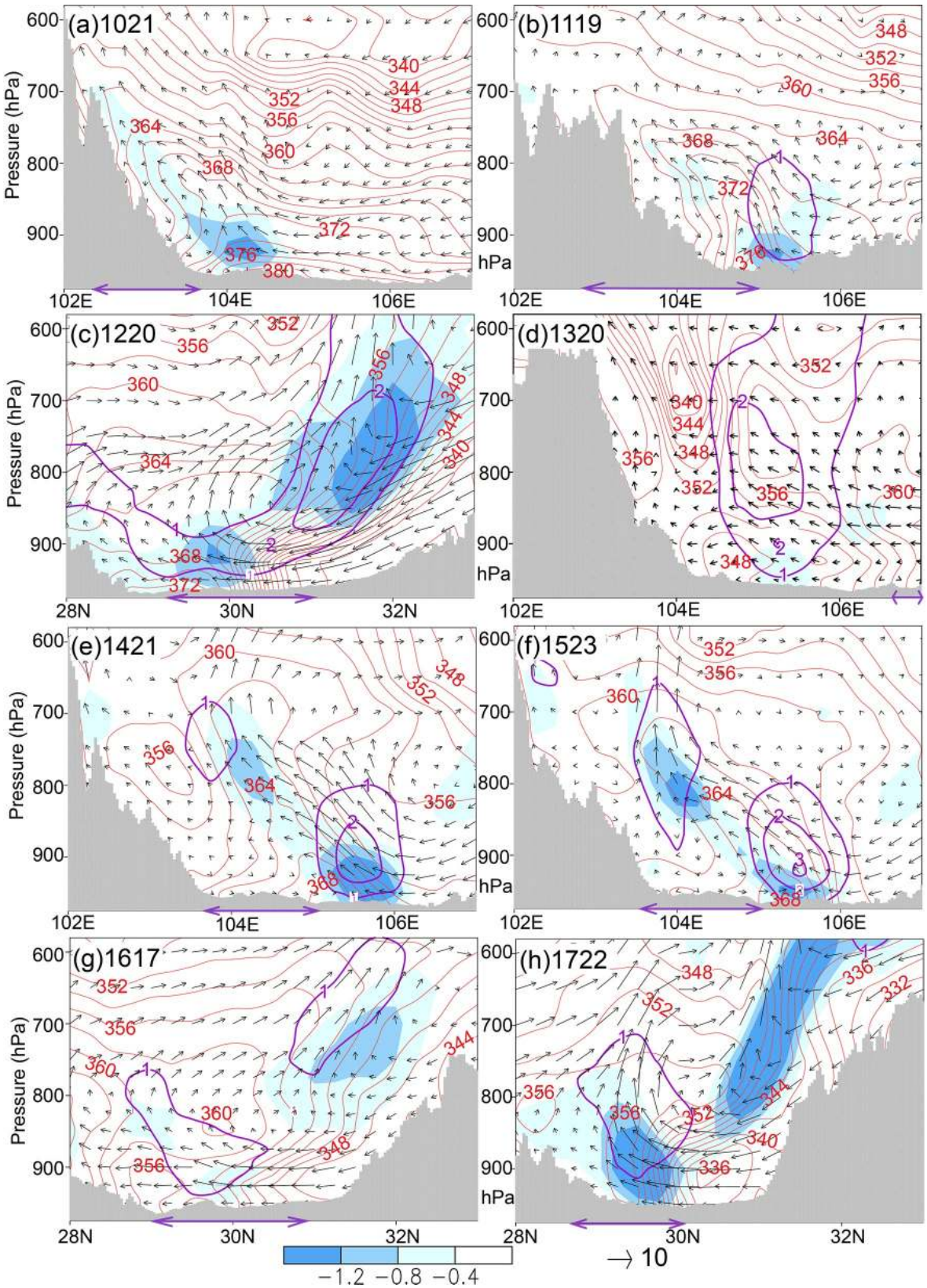

Fig. 15. Zonal (a, b, d, e, f) or meridional (c, g, h) vertical cross sections of the in-plane flow vectors [a composite of meridional/zonal wind (m s^{-1}) and veritical wind (cm s^{-1})], θ_{ep} (red-contoured at 2-K intervals), relative vorticity (purple contours of 1, 2 and 3 × 10^{-4} s^{-1}), and divergence of horizontal wind (blue shading, 10^{-4} s^{-1}) taken along the blue rectangles shown in Fig. 13 at the selected times. Gray shadings represent terrain. Purple double arrowed lines roughly indicate the location of convection initiation or strengthening during the evening hours shown in Fig. 13.

region. The westward extension of the anomalously strong subtropical high was conducive to the maintenance of the southerly LLJ in southwest China, which favored the transport of water vapor from lower latitudes to the basin, resulting in anomalously high precipitable water in the basin. The midlevel trough, albeit with weak negative anomalies, favored the advection of cold air into the target region and the quasi-geostrophic lifting of moist air ahead of the trough axis. In contrast, the western Pacific subtropical high was located more to the east during the E1 episode (from 1800 LST 10 August to 1700 LST 11 August), which was unfavorable for the development of a southerly LLJ to the southeast of the basin. Water vapor was transported into the basin from the south, east and west boundaries with roughly comparable strengths during E1.

The diurnal cycles of heavy rainfall during the E2 episode were closely related to those of the southerly LLJ in and to the southeast of the target region where the low-level wind oscillated periodically. The net water vapor flux from around the target area corresponded well to the diurnal variation of the LLJ and the intensity of the regionally averaged hourly rainfall rates, suggesting the importance of external water vapor supply for this persistent heavy rainfall event. Water vapor mainly entered the target area from the southern boundary, followed by the eastern boundary, with the strongest centers located at 800 and 900 hPa, respectively. The periodic variation of the southerly LLJ resulted in the evident diurnal cycles of the water vapor flux at the southern boundary of the target region, i.e., it strengthened at night and weakened during the daytime. Both the inertial oscillation mechanism and terrain thermal forcing played significant roles in the diurnal cycles of the LLJ in this extreme rainfall event. In addition, along with the variation of the wind direction and speed in the basin, wind convergence was enhanced over the southwest and the northwest of the basin during the evening hours, which was consistent with the heavy rainfall generation.

Results show that convective clouds were initiated over the plateau to the west of the target region in the afternoon during most days of the E2 episode. Their eastward movement and merging with the local convection enhanced the nocturnal rainfall in the basin, which was consistent with previous statistical studies (e.g., Bao et al., 2011; Qian et al., 2015). A more important contribution to the nighttime rainfall enhancement in the basin came from the locally initiated convection in the southwest of the basin in the evening hours, and the subsequent convection intensification in the southwest and northwest parts of the basin at nighttime. The southwest part of the basin was prone to convective initiation during the evening hours because of the presence of low-level wind convergence with high CAPE, and small dew-point depression at the surface.

There are mainly two mechanisms whereby convective initiation was facilitated in the basin during the evening hours of the E2 episode. The first mechanism was closely associated with cold air advection in the northern part of the basin. The cold airflow converged with and lifted warm, moist air in the basin, leading to convective initiation and the release of convective instability. The other mechanism played a role after the MCSs over the western Sichuan Plateau in the late afternoon moved into the western basin. The associated rain-evaporation cooling plus radiative cooling of the near-surface air after sunset led to the formation of a neutral to stable layer over the western mountain sloping surfaces and the adjacent basin area. It is the slantwise ascending motion of the warm, moist airflow from the southeast over the stable layer that triggered convection and released convective instability. Meanwhile, the low-level convergence associated with the southwest vortex facilitated the upward motion in E2. By comparison, the convective initiation during the E1 episode was mainly due to terrain lifting of conditionally unstable air over a wide coverage in the target region.

In other words, the daytime convective clouds over the western Sichuan Plateau contributed to the nocturnal peak rainfall production in the basin, not only through dropping heavy rainfall at night during their eastward journey into the basin, but also by rain evaporative cooling over the western sloping terrain whose cold airflow assisted in convective convection when interacting with warm, moist air over the southwestern basin during the evening hours.

In conclusion, we may emphasize, as Z19 did, the key roles of the southerly LLJ in the generation and enhancement of nocturnal heavy rainfall over the Sichuan basin during the 8-day period of 10–18 August 2020. Moreover, this case study indicates the importance of daytime convection over the western Sichuan Plateau and of cold air advection from the north in determining nocturnal convective initiation in the western basin. Of course, there are still many issues associated with the 8-day heavy rainfall events that are worthy of further investigation, such as the structures and evolution of cold boundaries, warm-moist airflows, and the impact of complex topography on the LLJ in the basin.

Acknowledgements. This study was supported by the National Natural Science Foundation of China (Grant Nos. 41775050, 91937301, 41775002, 42005008) and the Science Development Fund of Chinese of Academy of Meteorological Sciences (2020KJ022).

REFERENCES

Bao, X. H., F. Q. Zhang, and J. H. Sun, 2011: Diurnal variations of warm-season precipitation east of the Tibetan Plateau over China. *Mon. Wea. Rev.*, **139**, 2790–2810, https://doi.org/

10.1175/MWR-D-11-00006.1.

Blackadar, A. K., 1957: Boundary layer wind maxima and their significance for the growth of nocturnal inversions. *Bull. Amer. Meteor. Soc.*, **38**, 283–290, https://doi.org/10.1175/1520-0477-38.5.283.

Buajitti, K., and A. K. Blackadar, 1957: Theoretical studies of diurnal wind-structure variations in the planetary boundary layer. *Quart. J. Roy. Meteor. Soc.*, **83**, 486–500, https://doi.org/10.1002/qj.49708335804.

Chen, J., Y. G. Zheng, X. L. Zhang, and P. J. Zhu, 2013: Distribution and diurnal variation of warm-season short-duration heavy rainfall in relation to the MCSs in China. *Acta Meteorologica Sinica*, **27**, 868–888, https://doi.org/10.1007/s13351-013-0605-x.

Du, Y., and R. Rotunno, 2014: A simple analytical model of the nocturnal low-level jet over the Great Plains of the United States. *J. Atmos. Sci.*, **71**, 3674–3683, https://doi.org/10.1175/JAS-D-14-0060.1.

Feng, X. Y., C. H. Liu, G. Z. Fan, X. D. Liu, and C. Y. Feng, 2016: Climatology and structures of southwest vortices in the NCEP climate forecast system reanalysis. *J. Climate*, **29**, 7675–7701, https://doi.org/10.1175/JCLI-D-15-0813.1.

Fu, S.-M., J.-P. Zhang, J.-H. Sun, and X.-Y. Shen, 2014: A fourteen-year climatology of the southwest vortex in Summer. *Atmos. Ocean. Sci. Lett.*, **7**, 510–514, https://doi.org/10.3878/AOSL20140047.

Fu, S.-M., Z. Mai, J.-H. Sun, W.-L. Li, Y. Ding, and Y.-Q. Wang, 2019: Impacts of convective activity over the Tibetan Plateau on plateau vortex, southwest vortex, and downstream precipitation. *J. Atmos. Sci.*, **76**, 3803–3830, https://doi.org/10.1175/JAS-D-18-0331.1.

Hersbach, H., B. Bill, P. Berrisford, et al, 2020: The ERA5 global reanalysis. *Q. J. R. Meteorol. Soc*, **146**(730), 1999–2049, https://doi.org/10.1002/qj.3803.

Holton, J. R., 1967: The diurnal boundary layer wind oscillation above sloping terrain. *Tellus*, **19**, 200–205, https://doi.org/10.3402/tellusa.v19i2.9766.

Hoxit, L R., 1975: Diurnal variations in planetary boundary-layer winds over land. *Bound.-Layer Meteorol.*, **8**, 21–38, https://doi.org/10.1007/BF02579391.

Hu, L., D. F. Deng, S. T. Gao, and X. D. Xu, 2016: The seasonal variation of Tibetan convective systems: Satellite observation. *J. Geophys. Res.*, **121**, 5512–5525, https://doi.org/10.1002/2015JD024390.

Huang, Y. J., Y. B. Liu, Y. W. Liu, and J. C. Knievel, 2019: Budget analyses of a record-breaking rainfall event in the coastal metropolitan city of Guangzhou, China. *J. Geophys. Res.*, **124**, 9391–9406, https://doi.org/10.1029/2018JD030229.

Jiang, X. N., N.-C. Lau, I. M. Held, and J. J. Ploshay, 2007: Mechanisms of the Great Plains low-level jet as simulated in an AGCM. *J. Atmos. Sci.*, **64**, 532–547, https://doi.org/10.1175/JAS3847.1.

Jin, X., T. W. Wu, and L. Li, 2013: The quasi-stationary feature of nocturnal precipitation in the Sichuan Basin and the role of the Tibetan Plateau. *Climate Dyn.*, **41**, 977–994, https://doi.org/10.1007/s00382-012-1521-y.

Kuo, Y.-H., L. S. Cheng, and J.-W. Bao, 1988: Numerical simulation of the 1981 Sichuan flood. *Part I: Evolution of a mesoscale southwest vortex. Mon. Wea. Rev.*, **116**, 2481–2504, https://doi.org/10.1175/1520-0493(1988)116<2481:NSOTSF>2.0.CO;2.

Li, J., J. Du, D.-L. Zhang, C. G. Cui, and Y. S. Liao, 2014: Ensemble-based analysis and sensitivity of mesoscale forecasts of a vortex over southwest China. *Quart. J. Roy. Meteor. Soc.*, **140**, 766–782, https://doi.org/10.1002/qj.2200.

Li, L., R. H. Zhang, and M. Wen, 2017: Genesis of southwest vortices and its relation to Tibetan Plateau vortices. *Quart. J. Roy. Meteor. Soc.*, **143**, 2556–2566, https://doi.org/10.1002/qj.3106.

Li, Y. D., Y. Wang, Y. Song, L. Hu, S. T. Gao, and F. Rong, 2008: Characteristics of summer convective systems initiated over the Tibetan Plateau. *Part I: Origin*, **track**–2695, https://doi.org/10.1175/2008JAMC1695.1.

Liu, X., Y. L. Luo, Z. Y. Guan, and D.-L. Zhang, 2018: An extreme rainfall event in coastal South China during SCMREX-2014: Formation and roles of rainband and echo trainings. *J. Geophys. Res.*, **123**, 9256–9278, https://doi.org/10.1029/2018JD028418.

Luo, Y. L., M. W. Wu, F. M. Ren, J. Li, and W.-K. Wong, 2016: Synoptic situations of extreme hourly precipitation over China. *J. Climate*, **29**, 8703–8719, https://doi.org/10.1175/JCLI-D-16-0057.1.

Luo, Y. L., and Coauthors, 2020: Science and prediction of heavy rainfall over China: Research progress since the reform and opening-up of new China. *Journal of Meteorological Research*, **34**, 427–459, https://doi.org/10.1007/s13351-020-0006-x.

Markowski, P., and Y. Richardson, 2010: *Mesoscale Meteorology in Midlatitudes*. *John Wiley & Sons*, **Ltd.**, 407pp, https://doi.org/10.1002/9780470682104.

Qian, T. T., P. Zhao, F. Q. Zhang, and X. H. Bao, 2015: Rainy-season precipitation over the Sichuan basin and adjacent regions in southwestern China. *Mon. Wea. Rev.*, **143**, 383–394, https://doi.org/10.1175/MWR-D-13-00158.1.

Shapiro, A., E. Fedorovich, and S. Rahimi, 2016: A unified theory for the Great Plains nocturnal low-level jet. *J. Atmos. Sci.*, **73**, 3037–3057, https://doi.org/10.1175/JAS-D-15-0307.1.

Sugimoto, S., and K. Ueno, 2010: Formation of mesoscale convective systems over the eastern Tibetan Plateau affected by plateau-scale heating contrasts. *J. Geophys. Res.*, **115**(D16), D16105, https://doi.org/10.1029/2009JD013609.

Tu, C.-C., Y.-L. Chen, S.-Y. Chen, Y.-H. Kuo, and P.-L. Lin, 2017: Impacts of including rain-evaporative cooling in the initial conditions on the prediction of a coastal heavy rainfall event during TiMREX. *Mon. Wea. Rev.*, **145**, 253–277, https://doi.org/10.1175/MWR-D-16-0224.1.

Ueno, K., S. Sugimoto, T. Koike, H. Tsutsui, and X. D. Xu, 2011: Generation processes of mesoscale convective systems following midlatitude troughs around the Sichuan basin. *J. Geophys. Res.*, **116**, D02104, https://doi.org/10.1029/2009JD013780.

Wang, C.-C., Chen, G. T.-J., and R. E. Carbone, 2005: Variability of warm-season cloud episodes over East Asia based on GMS infrared brightness temperature observations. *Mon. Wea. Rev.*, **133**, 1478–1500, https://doi.org/10.1175/MWR2928.1.

Wang, Q.-W., and Z.-M. Tan, 2014: Multi-scale topographic control of southwest vortex formation in Tibetan Plateau region in an idealized simulation. *J. Geophys. Res.*, **119**, 11543–11561, https://doi.org/10.1002/2014JD021898.

Wu, M. W., and Y. L. Luo, 2016: Mesoscale observational analysis of lifting mechanism of a warm-sector convective sys-

tem producing the maximal daily precipitation in China mainland during pre-summer rainy season of 2015. *Journal of Meteorological Research*, **30**, 719–736, https://doi.org/10.1007/s13351-016-6089-8.

Xia, R. D., D.-L. Zhang, and B. L. Wang, 2015: A 6-yr cloud-to-ground lightning climatology and its relationship to rainfall over Central and Eastern China. *J. Appl. Meteorol. Climatol.*, **54**, 2443–2460, https://doi.org/10.1175/JAMC-D-15-0029.1.

Yuan, W. H., R. C. Yu, M. H. Zhang, W. Y. Lin, H. M. Chen, and J. Li, 2012: Regimes of diurnal variation of summer rainfall over subtropical East Asia. *J. Climate*, **25**, 3307–3320, https://doi.org/10.1175/JCLI-D-11-00288.1.

Zhang, C. H., R. D. Xia, and Y. Q. Wang, 2018: Observational analysis of a local heavy rainfall in Beijing caused by terrain, cold pool outflow and warm moist air interactions. *Transactions of Atmospheric Sciences*, **41**, 207–219, https://doi.org/10.13878/j.cnki.dqkxxb.20160115001. (in Chinese with English abstract)

Zhang, D.-L., and J. M. Fritsch, 1987: Numerical simulation of the meso-β scale structure and evolution of the 1977 Johnstown flood. *Part II: Inertially stable warm-core vortex and the mesoscale convective complex. J. Atmos. Sci.*, **44**, 2593–2612, https://doi.org/10.1175/1520-0469(1987)044<2593:NSOTMS>2.0.CO;2.

Zhang, D.-L., S. L. Zhang, and S. J. Weaver, 2006: Low-level jets over the mid-Atlantic States: Warm-season climatology and a case study. *J. Appl. Meteorol. Climatol.*, **45**, 194–209, https://doi.org/10.1175/JAM2313.1.

Zhang, Y. H., M. Xue, K. F. Zhu, and B. W. Zhou. 2019: What is the main cause of diurnal variation and nocturnal peak of summer precipitation in Sichuan Basin, China? The key role of boundary layer low-level jet inertial oscillations. *J. Geophys. Res.*, **124**, 2643–2664, https://doi.org/10.1029/2018JD029834.

Zhao, Y. C., 2015: A study on the heavy-rain-producing mesoscale convective system associated with diurnal variation of radiation and topography in the eastern slope of the western Sichuan plateau. *Meteorol. Atmos. Phys.*, **127**, 123–146, https://doi.org/10.1007/s00703-014-0356-y.

Zhou, T.-J., and R.-C. Yu, 2005: Atmospheric water vapor transport associated with typical anomalous summer rainfall patterns in China. *J. Geophys. Res.*, **110**, D08104, https://doi.org/10.1029/2004JD005413.